Organic Electronics 57 (2018) 206–210

Contents lists available at ScienceDirect

Organic Electronics

journal homepage: www.elsevier.com/locate/orgel

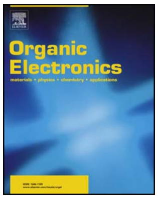

Improved performance of perovskite photodetectors based on a solution-processed $CH_3NH_3PbI_3/SnO_2$ heterojunction

Hairuo Wu[a,b], Zisheng Su[a,c,*], Fangming Jin[a], Haifeng Zhao[a], Wenlian Li[a], Bei Chu[a,**]

[a] State Key Laboratory of Luminescence and Applications, Changchun Institute of Optics, Fine Mechanics and Physics, Chinese Academy of Sciences, Changchun, 130033, PR China
[b] University of Chinese Academy of Sciences, Beijing, 100039, PR China
[c] College of Physics and Information Engineering, Quanzhou Normal University, Quanzhou, 362000, PR China

ARTICLE INFO

Keywords:
Perovskite photodetector
Heterojunction
Exciton dissociation
Charge transfer

ABSTRACT

High-performance perovskite photodetectors are demonstrated based on a $CH_3NH_3PbI_3/SnO_2$ heterojunction on glass substrates. This heterojunction can be fabricated with a facile and low-cost spin-coating method at low temperature. The photoresponse of the photodetectors is dramatically increased with such a heterojunction structure. The optimized device shows a responsivity of 1.65 A/W, which is more than twice to the reference device with a $CH_3NH_3PbI_3$ layer on bare glass (0.67 A/W). Besides, the device also exhibits a fast response speed with rise and decay times both of about 10 ms. The inserted SnO_2 layer not only improves the morphology and crystallinity of the $CH_3NH_3PbI_3$ films but also increases the dissociation efficiency of the excitons in $CH_3NH_3PbI_3$ through electron transfers from $CH_3NH_3PbI_3$ to SnO_2, which increases the hole collection efficiency due to the suppressed charge carrier recombination probability of the devices and prolonged lifetime of the holes in $CH_3NH_3PbI_3$ films.

1. Introduction

Hybrid organolead halide perovskites $CH_3NH_3PbX_3$ (X = Cl, Br, I) have received a great attention in applications in light-emitting diodes [1,2], solar cells [3–5], photodetectors [6,7], and lasers [8] due to their large absorption coefficient, high carrier mobility, long exciton diffusion length, and low-temperature fabrication process [9–15]. These tremendous intrinsic properties make them more suitable as light absorption materials for solar cells and a power conversion efficiency (PCE) of 22% have been realized recently [16]. Apart from solar cells, perovskite photodetectors have drawn more attention since the first device was reported in 2014 [17–27]. The working of a photodetector involves the formation of excitons after photon absorption, the dissociation of excitons into electrons and holes, and the collection of electrons and holes by the electrodes. Numerous methods have been reported to improve the performance of the devices. Zhang et al. demonstrated increased absorption efficiency of the perovskite photodetectors through controlling the morphology of the $CH_3NH_3PbI_3$ perovskite films [28]. Zhao et al. optimized the electrode materials to increase the charge carrier collection efficiency [29]. The charge carrier collection efficiency can also be improved by introducing a MoO_3 buffer layer at the Au/$CH_3NH_3PbI_3$ interface [30]. For a lateral perovskite photodetector based on pristine perovskite film, the dissociation of excitons is derived by the forces of built-in internal electric field and/or applied external electrical field. To increase the exciton dissociation efficiency, a heterojunction has been adopted. For example, two dimensional materials graphene [31] and MoS_2 [32] have been selected to construct heterojunction perovskite photodetectors and high performance is demonstrated. On the other hand, nanostructured metal oxides have also been exploited, such as ZnO nanowires [33,34] and TiO_2 nanotubes [35]. However, the synthesis of the two dimensional and nanostructure materials is very complicated and expensive.

SnO_2 is an n-type semiconductor and can form a smooth and homogenous film via a facial and low-cost spin-coating method at a low temperature. Recently, it has been adopted as the electron-transporting material for perovskite solar cells. Because of its suitable energy levels in alignment with $CH_3NH_3PbI_3$, efficient electron transfer from $CH_3NH_3PbI_3$ to SnO_2 occurs and high PCE has been demonstrated [36–43]. In this work, spin-casted SnO_2 films from an aqueous solution is combined with $CH_3NH_3PbI_3$ to form heterojunction perovskite photodetectors. The device with an optimized SnO_2 layer achieves a responsivity of 1.65 A/W with a fast response speed with rise and decay

---

[*] Corresponding author. State Key Laboratory of Luminescence and Applications, Changchun Institute of Optics, Fine Mechanics and Physics, Chinese Academy of Sciences, Changchun, 130033, PR China.

[**] Corresponding author.

E-mail addresses: suzs@ciomp.ac.cn (Z. Su), chub@ciomp.ac.cn (B. Chu).

https://doi.org/10.1016/j.orgel.2018.03.018
Received 3 January 2018; Received in revised form 6 March 2018; Accepted 9 March 2018

times both of about 10 ms. The performance is dramatically higher than the reference device with a pristine $CH_3NH_3PbI_3$ layer on bare glass.

2. Experimental section

All chemicals were purchased commercially and used as received. $CH_3NH_3PbI_3$ was synthesized by mixing CH_3NH_3I and PbI_2 at 1:1 (0.162:0.462 g) equimolar ratio in N, N-dimethylformamide (DMF, 0.7 ml) and dimethyl sulfoxide (DMSO, 0.3 ml) at 70 °C, stirring for 12 h inside a nitrogen-filled glove box. Glass substrates were cleaned by ultra-sonication in acetone, deionized water, and acetone for 10 min, respectively, and dried naturally. Then they were treated in an ultraviolet-ozone chamber for 10 min before deposition of the SnO_2 layer. The devices were fabricated by spin-coating of the SnO_2 aqueous solution onto the pre-cleaned glass substrates with different rate and then annealing at 150 °C for 30 min, which forms SnO_2 layers with different thicknesses. The substrates were then loaded into the glove box, followed by spin-coating the as-synthesized $CH_3NH_3PbI_3$ precursor solution on them with a rate of 500 rpm for 5 s and 3000 rpm for 60 s. After 20 s delay, 300 μl chlorobenzene was quickly added during the spin-coating procedure. The substrates were then annealed at 70 and 105 °C for 2 and 10 min, respectively. During the annealing process, the color of the $CH_3NH_3PbI_3$ films changed from light yellow to black, indicating that the ABO_3 structure was gradually formed at high temperature during the evaporation of the DMF and DMSO solvents. Au electrodes were thermally deposited onto the $CH_3NH_3PbI_3$ films in a vacuum chamber at a pressure of $\sim 4 \times 10^{-4}$ Pa through a shadow mask, defining the channel length and width of 1000 and 60 μm, respectively.

X-ray diffraction (XRD) pattern was measured with a diffractometer (Rigaku D/ Max- 2500) using Cu Kα radiation ($\lambda = 1.54056$ Å). The current-voltage (I-V) characteristics were measured using a programmable source meter (Keithley 2400) under illumination of an AM 1.5G solar simulator (Newport 94023A) with an intensity of 100 mW/cm^2. Scanning electron microscopy (SEM) images were measured on a Hitachi S4800. Absorption spectra were recorded with a Shimadzu UV-3101PC spectrophotometer. The external quantum efficiency (EQE) data was measured with a Stanford SR803 lock-in amplifier under monochromatic illumination at a chopping frequency of 130 Hz by a Stanford SR540 chopper. All measurements were performed under ambient conditions and at room temperature.

3. Results and discussion

The spin-casted SnO_2 films exhibit a smooth and homogenous morphology, as shown in Fig. S1. The thicknesses of the SnO_2 films decrease with the increased spin-coating rate and they are about 140, 120, and 90 nm for the films with a spin-coating rates of 3000, 4000, and 5000 rpm, respectively (Fig. S2). The surface morphology and cross-sectional images of the $CH_3NH_3PbI_3$ films on glass and SnO_2 films are shown in Figs. 1 and 2. The average grain sizes of all the $CH_3NH_3PbI_3$ films are all about 500 nm, and this large grain size can reduce the grain boundary and hence increase the charge carrier collection efficiency. However, some pin-holes can be found for the $CH_3NH_3PbI_3$ film on bare glass, while a more compacted and homogenous morphology is found for the films on SnO_2. This suggests that the SnO_2 facilitates the growth of the perovskite films, which is one of the reasons that the perovskite solar cells with a SnO_2 electron-transporting layer can achieve a high PCE [36–43]. The thickness of the $CH_3NH_3PbI_3$ film on bare glass is about 650 nm. The $CH_3NH_3PbI_3$ films on 3000 and 4000 rpm SnO_2 films have a thickness comparable to that on bare glass, which are 670 and 630 nm, respectively. However, it dramatically decreases to 330 nm on 5000 rpm SnO_2 film. This discrepancy should be attributed to the altered surface properties of the SnO_2 films with decreased thickness.

Fig. 3 depicts the XRD patterns of the $CH_3NH_3PbI_3$ films on bare glass and SnO_2 films. The XRD patterns show obvious diffraction peaks at 14.26°, 28.34°, and 32.02°, which can be assigned to the reflections from (110), (220), and (310) crystal planes of $CH_3NH_3PbI_3$, respectively. No obvious diffraction peak of PbI_2 is observed for all the films, indicating a full conversion of PbI_2 to $CH_3NH_3PbI_3$. However, the full width at half maximum of the diffraction peak at 14.26° of the $CH_3NH_3PbI_3$ film on bare glass is 0.105°, while it reduces to 0.092°, 0.099°, and 0.096° for the films on 3000, 4000, and 5000 rpm SnO_2 films, respectively. This indicates that the crystallinity is improved for the films on SnO_2. The improved morphology and crystallinity are favorable to construct high-performance perovskite photodetectors.

Fig. 4 draws the absorption spectra of the $CH_3NH_3PbI_3$ films. All the films show a similar broad absorption band in the visible region with an edge of about 780 nm, corresponding to a band-gap of 1.59 eV. The film on 3000 rpm SnO_2 has a little higher absorption intensity than that on bare glass, which is consistent with the thickness of $CH_3NH_3PbI_3$ films shown in Fig. 2. As SnO_2 primary absorbs at ultraviolet regions due to its large band-gap (Fig. S3), the different absorption intensity can be attributed to their different thickness and morphology.

Based on these $CH_3NH_3PbI_3$ films, lateral photodetectors with the structure shown in the inset of Fig. 5 are fabricated. Fig. 5 depicts the I-V characteristics of the photodetectors under illumination of an AM 1.5G solar simulator with an intensity of 100 mW/cm^2. All the devices present a nearly linear I-V curve under illumination, indicating the formation of Ohmic contact between $CH_3NH_3PbI_3$ and Au electrodes. The photocurrent of the device on bare glass is about 1.0 μA at ± 10 V. The photocurrent is dramatically increased for the devices on SnO_2 layers. The device on 3000 rpm SnO_2 achieves a photocurrent of 2.23 μA, which is more than twice to that of the reference device on bare glass. Moreover, all the devices show no obvious hysteresis for the I-V curves with different scan directions (Fig. S4), which indicates the high reliability of these devices for practical applications. Besides, the devices also exhibit a high reproducibility, as shown in Table S1 with the data averaged from 6 devices with the same device configurations.

The responsivity (R) of a photodetector is defined as:

$$R = \Delta I / PS \tag{1}$$

where ΔI ($\Delta I = I_{photo} - I_{dark}$) is the difference between the photocurrent and dark current, P is the incident light intensity, and S is the effective illumination area. Fig. 6 shows the R of the photodetectors at 1 V derived from their EQE spectra. All the devices display a broad photoresponse from 350 to 800 nm, which is consistent with their absorption spectra shown in Fig. 4. The device on 3000 rpm SnO_2 has the highest R in the whole response wavelengths, which is attributed to its highest photocurrent. A maximum R of 1.65 A/W is obtained at 705 nm, while it is only 0.76 A/W for the reference device on bare glass, confirming the improved photocurrent of the device with a $CH_3NH_3PbI_3/SnO_2$ heterojunction.

As demonstrated in Figs. 1 and 3, the morphology and crystallinity of the $CH_3NH_3PbI_3$ films on SnO_2 layers are improved. These would result in enhanced exciton diffusion length and charge carrier mobility and hence the photocurrent of the devices. On the other hand, the $CH_3NH_3PbI_3$ film on 3000 rpm SnO_2 is 20 nm thicker than that on bare glass. This small difference in thickness has little contribution to the dramatically boosted photoresponse shown in Fig. 5. The energy levels of $CH_3NH_3PbI_3$ and SnO_2 are shown in the inset of Fig. 5 [37], which demonstrated that a heterojunction is formed between these two materials. Under illumination, excitons are generated in $CH_3NH_3PbI_3$ and then dissociated into free charge carriers derived by the force of applied external electrical field. The $CH_3NH_3PbI_3/SnO_2$ heterojunction will increase the exciton dissociation efficiency through electron transfers from $CH_3NH_3PbI_3$ to SnO_2 [44,45]. This can be further confirmed by the quenched photoluminescence of $CH_3NH_3PbI_3$ after inserting a SnO_2 layer [39–42]. The electron transfer process also suppresses the charge carrier recombination probability of the devices and prolongs the lifetime of holes in $CH_3NH_3PbI_3$ films. As a result, the photocurrent of the heterojunction devices is dramatically enhanced. The photocurrent is

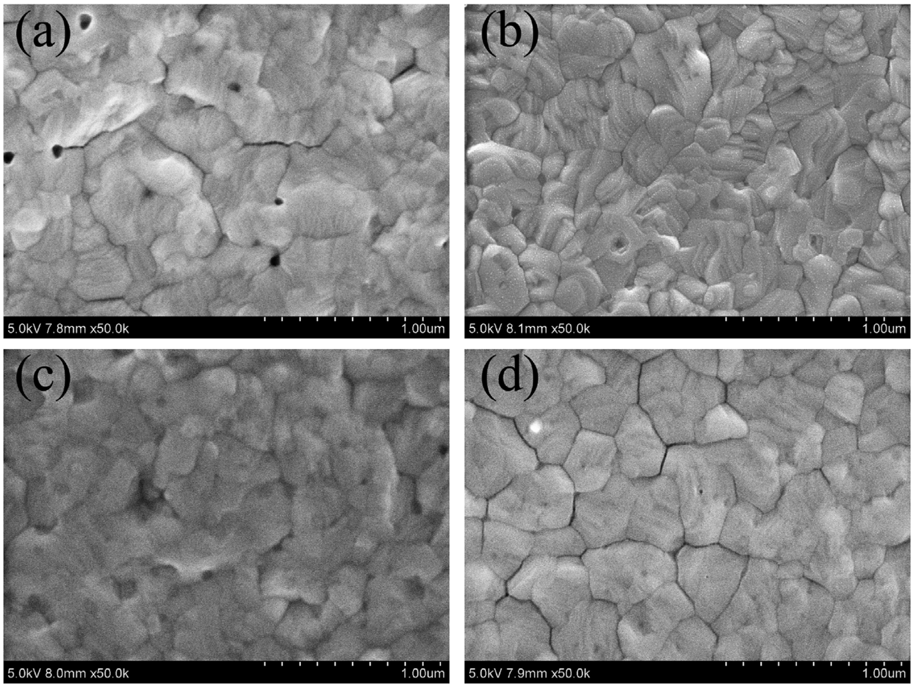

Fig. 1. Top-viewed SEM images of the $CH_3NH_3PbI_3$ films spin-coated on (a) bare ITO, (b) 3000 rpm SnO_2, (c) 4000 rpm SnO_2, and (d) 5000 rpm SnO_2, respectively.

decreased with thicker SnO_2 layers, which is attributed to the lower thickness of $CH_3NH_3PbI_3$ layers, as shown in Fig. 2. We should note that the SnO_2 layer is isolated, thus the electrons in SnO_2 layer are difficult to transport to the electrode, which may result in the accumulation of the photo-generated electrons in SnO_2 layer. Thus the improved responsivity of the devices should be attributed to their improved hole collection efficiency. On the other hand, non-excitonic nature of the perovskite materials has been proposed, and the excitons generated in the perovskite film will dissociated into free charge carriers immediately [46]. Even in such a mechanism, the photogenerated electrons in perovskites can also transfer to SnO_2 layer, which finally increases the photoresponse of the devices.

The detectivity (D^*) can be calculated by the following formula if the shot noise from the dark current is the major contribution [45]:

$$D* = R/\sqrt{2qJd} \tag{2}$$

where q is absolute electron charge and J_d ($J_d = I_{\text{dark}}/S$) is dark current density. The dark current of the devices are all below 10^{-10} A, which is beyond the precision limitation of Keithley 2400. However, the D^* is higher than 10^{12} Jones in the whole response region taking into account a dark current of 10^{-10} A.

Photoresponse speed is another figure of merit factor for a

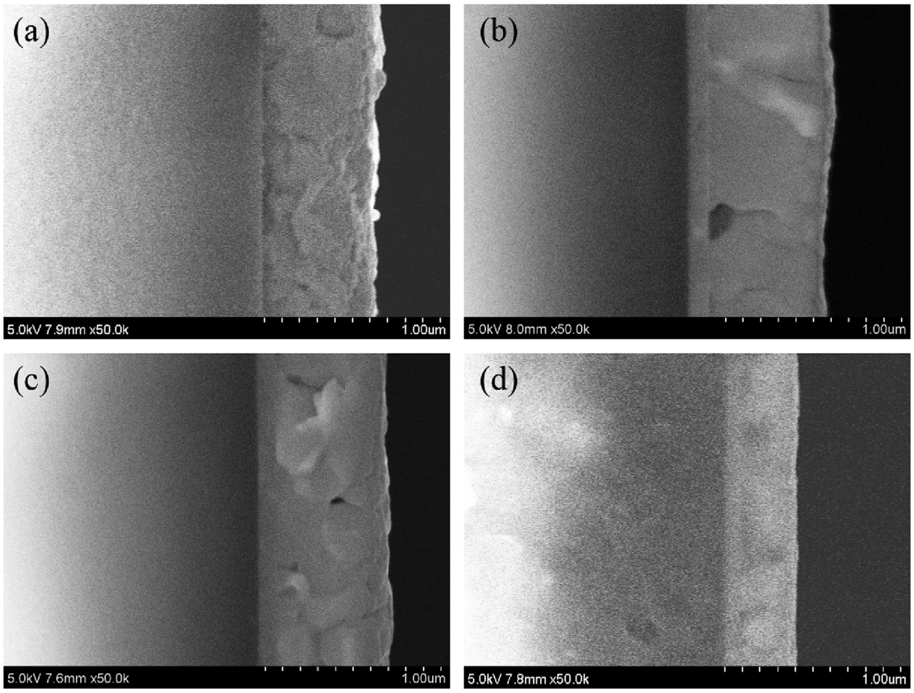

Fig. 2. Cross-sectional SEM images of the $CH_3NH_3PbI_3$ films spin-coated on (a) bare ITO, (b) 3000 rpm SnO_2, (c) 4000 rpm SnO_2, and (d) 5000 rpm SnO_2, respectively.

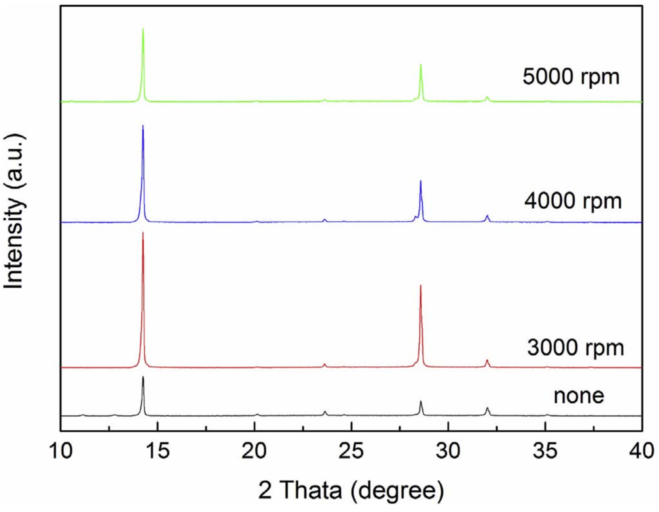

Fig. 3. XRD patterns of the $CH_3NH_3PbI_3$ films spin-coated on (a) bare ITO, (b) 3000 rpm SnO_2, (c) 4000 rpm SnO_2, and (d) 5000 rpm SnO_2, respectively.

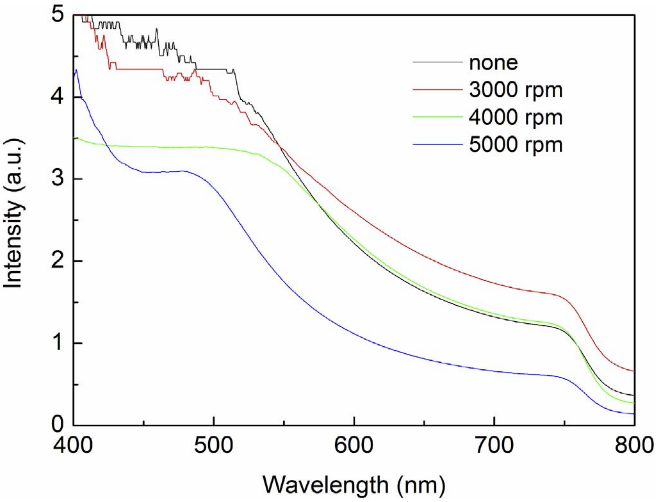

Fig. 4. Absorption spectra of the $CH_3NH_3PbI_3$ films spin-coated on (a) bare ITO, (b) 3000 rpm SnO_2, (c) 4000 rpm SnO_2, and (d) 5000 rpm SnO_2, respectively.

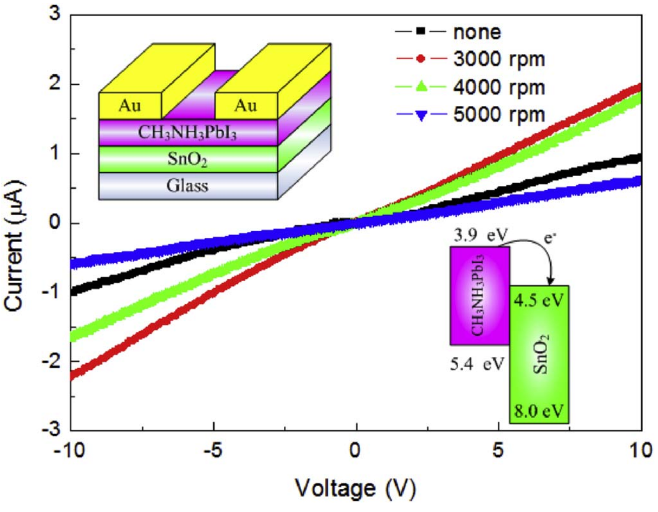

Fig. 5. I–V curves of the photodetectors with different SnO_2 layer under illumination of an AM 1.5G solar simulator with an intensity of 100 mW/cm^2. Inset: device structure of the photodetectors (upper) and work mechanism of the heterojunction photodetectors (lower).

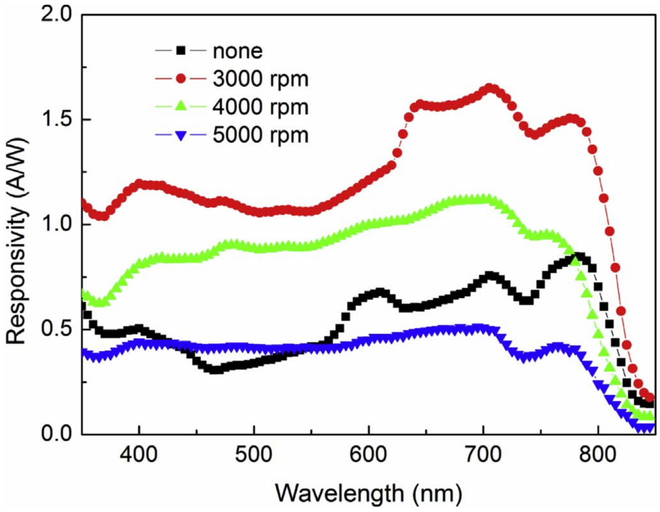

Fig. 6. Responsivity of the photodetectors with and without a SnO_2 layer.

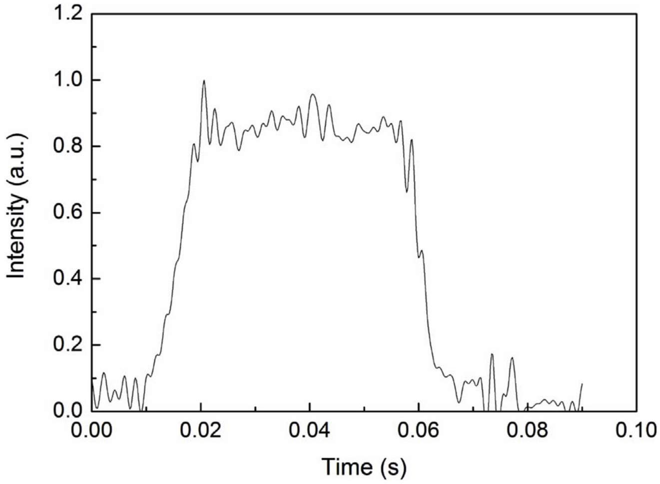

Fig. 7. Photoresponse behavior of the photodetector with a SnO_2 layer.

photodetector. The rise time and decay time are defined as the time taken for the initial current to increase to 90% of the peak value, or vice versa, respectively. The transient photoresponse behavior of the device on 3000 rpm SnO_2 is investigated under illumination of a white light with the light switched on and off at a bias voltage of 1 V, as shown in Fig. 7. The rise and decay times of the device are both about 10 ms. Such a response speed is one of the highest values among the reported heterojunction perovskite photodetectors [24,30,33].

4. Conclusion

In conclusion, electron transporting material SnO_2 is used to construct photodetectors by combining with a perovskite material $CH_3NH_3PbI_3$ and high-performance devices are demonstrated. These devices can be processed with a facile and low-cost spin-coating method at low temperature. The optimized photodetector exhibits high responsivity, detectivity, and fast response speed. A high responsivity of 1.65 A/W is obtained, which is more than twice to the reference device with a pristine $CH_3NH_3PbI_3$ layer on bare glass. The enhanced performance is attributed to the simultaneous improved morphology and crystallinity of the $CH_3NH_3PbI_3$ films as well as the increased exciton dissociation efficiency in $CH_3NH_3PbI_3$ through electron transfers from $CH_3NH_3PbI_3$ to SnO_2, which suppresses the charge carrier recombination probability of the devices and prolongs the lifetime of holes in $CH_3NH_3PbI_3$ films. These results suggest that the introduction of a heterojunction to the $CH_3NH_3PbI_3$ based photodetector is a promising strategy to enhance the performance of the device. Such a structure may have potential applications in constructing high performance and low-cost perovskite photodetectors.

Acknowledgements

This work was supported by the National Natural Science Foundation of China (61575192 and 61604149), the Science and Technology Development Plan of Jilin Province (20170520130JH), and the project of Jiangsu Key Laboratory for Carbon-Based Functional Materials and Devices (KJS1615).

Appendix A. Supplementary data

Supplementary data related to this article can be found at http://dx.doi.org/10.1016/j.orgel.2018.03.018.

References

[1] Z.-K. Tan, R.S. Moghaddam, M.L. Lai, P. Docampo, R. Higler, F. Deschler, M. Price, A. Sadhanala, L.M. Pazos, D. Credgington, F. Hanusch, T. Bein, H.J. Snaith, R.F. Friend, Bright light-emitting diodes based on organometal halide perovskite, Nat. Nanotechnol. 9 (2014) 687–692.

[2] N. Wang, L. Cheng, R. Ge, S. Zhang, Y. Miao, W. Zou, C. Yi, Y. Sun, Y. Gao, R. Yang, Y. Wei, Q. Guo, Y. Ke, M. Yu, Y. Jin, Y. Liu, Q. Ding, D. Di, L. Yang, G. Xing, H. Tian, C. Jin, F. Gao, R.H. Friend, J. Wang, W. Huang, Perovskite light-emitting diodes based on solution-processed self-organized multiple quantum wells, Nat. Photon. 10 (2016) 699–704.

[3] A. Kojima, K. Teshima, Y. Shirai, T. Miyasaka, J. Am. Chem. Soc. 131 (2009) 6050–6051.

[4] F. Hou, Z. Su, F. Jin, X. Yan, L. Wang, H. Zhao, J. Zhu, B. Chu, W. Li, Efficient and stable planar heterojunction perovskite solar cells with an MoO_3/PEDOT: PSS hole transporting layer, Nanoscale 7 (2015) 9427–9432.

[5] S. Li, B. Yang, R. Wu, C. Zhang, C. Zhang, X.-F. Tang, G. Liu, P. Liu, C. Zhou, Y. Gao, J.-Q. Meng, J. Yang, High-quality $CH_3NH_3PbI_3$ thin film fabricated via intramolecular exchange for efficient planar heterojunction perovskite solar cells, Org. Electron. 39 (2016) 304–310.

[6] M. Ahmadi, T. Wu, B. Hu, A review on organic-Inorganic halide perovskite photodetectors: device engineering and fundamental physics, Adv. Mater. 29 (2017) 1605242.

[7] Y. Dong, Y. Zou, J. Song, X. Song, H. Zeng, Recent progress of metal halide perovskite photodetectors, J. Mater. Chem. C 5 (2017) 11369–11394.

[8] G. Xing, N. Mathews, S.S. Lim, N. Yantara, X. Liu, D. Sabba, M. Grätzel, S. Mhaisalkar, T.C. Sun, Low-temperature solution-processed wavelength-tunable perovskites for lasing, Nat. Mater. 13 (2014) 476–480.

[9] A. Marchioro, J. Teuscher, D. Friedrich, M. Kunst, R. van de Krol, T. Moehl, M. Gratzel, J.E. Moser, Unravelling the mechanism of photoinduced charge transfer processes in lead iodide perovskite solar cells, Nat. Photon. 8 (2014) 250–255.

[10] S.D. Stranks, G.E. Eperon, G. Grancini, C. Menelaou, M.J.P. Alcocer, T. Leijtens, L.M. Herz, A. Petrozza, H.J. Snaith, Electron-hole diffusion lengths exceeding 1 micrometer in an organometal trihalide perovskite absorber, Science 342 (2013) 341–344.

[11] G.C. Xing, N. Mathews, S.Y. Sun, S.S. Lim, Y.M. Lam, M. Grätzel, S. Mhaisalkar, T.C. Sum, Long-range balanced electron- and hole-transport lengths in organic-inorganic $CH_3NH_3PbI_3$, Science 342 (2013) 344–347.

[12] H. Zhou, Q. Chen, G. Li, S. Luo, T.B. Song, H.S. Duan, Z. Hong, J. You, Y. Liu, Y. Yang, Interface engineering of highly efficient perovskite solar cells, Science 345 (2014) 542–546.

[13] N.J. Jeon, J.H. Noh, W.S. Yang, Y.C. Kim, S. Ryu, J. Seo, S.I. Seok, Compositional engineering of perovskite materials for high-performance solar cells, Nature 517 (2015) 476–480.

[14] W.S. Yang, J.H. Noh, N.J. Jeon, Y.C. Kim, S. Ryu, J. Seo, S.I. Seok, High-performance photovoltaic perovskite layers fabricated through intramolecular exchange, Science 348 (2015) 1234–1237.

[15] N. Arora, M.I. Dar, A. Hindderhofer, N. Pellet, F. Schreiber, S.M. Zakeeruddin, M. Grätzel, Perovskite solar cells with CuSCN hole extraction layers yield stabilized efficiencies greater than 20%, Science 358 (2017) 768–771.

[16] W.S. Yang, B.-W. Park, E.H. Jung, N.J. Jeon, Y.C. Kim, D.U. Lee, S.S. Shin, J. Seo, E.K. Kim, J.H. Noh, S.I. Seok, Iodide management in formamidinium-lead-halide-based perovskite layers for efficient solar cells, Science 356 (2017) 1376–1379.

[17] X. Hu, X.D. Zhang, L. Liang, J. Bao, S. Li, W.L. Yang, Y. Xie, High-performance flexible broadband photodetector based on organolead halide perovskite, Adv. Funct. Mater. 24 (2014) 7373–7380.

[18] L.T. Dou, Y. Yang, J.B. You, Z.R. Hong, W.H. Chang, G. Li, Y. Yang, Solution-processed hybrid perovskite photodetectors with high detectivity, Nat. Commun. 5 (2014) 5404.

[19] H.R. Xia, J. Li, W.T. Sun, L.M. Peng, Organohalide lead perovskite based photodetectors with much enhanced performance, Chem. Commun. 50 (2014) 13695–13697.

[20] R. Dong, Y. Fang, J. Chae, J. Dai, Z. Xiao, Q. Dong, Y. Yuan, A. Centrone, X.C. Zeng, J. Huang, High-gain and low-driving-voltage photodetectors based on organolead triiodide perovskites, Adv. Mater. 27 (2015) 1912–1918.

[21] F. Wang, J. Mei, Y. Wang, L. Zhang, H. Zhao, D. Zhao, Fast photoconductive responses in organometal halide perovskite photodetectors, ACS Appl. Mater. Interfaces 8 (2016) 2840–2846.

[22] H. Liu, X. Zhang, L. Zhang, Z. Yin, D. Wang, J. Meng, Q. Jiang, Y. Wang, J. You, J. Mater. Chem. C 5 (2017) 6115–6122.

[23] L. Zhou, K. Yu, F. Yang, H. Cong, N. Wang, J. Zhang, Y. Zuo, C. Li, B. Cheng, Q. Wang, J. Mater. Chem. C 5 (2017) 6224–6233.

[24] S. Tong, H. Wu, C. Zhang, S. Li, C. Wang, J. Shen, S. Xiao, J. He, J. Yang, J. Sun, Y. Gao, Large-area and high-performance $CH_3NH_3PbI_3$ perovskite photodetectors fabricated via doctor blading in ambient condition, Org. Electron. 49 (2017) 347–354.

[25] Y. Liu, F. Li, C.P. Veeramalai, W. Chen, T. Guo, C. Wu, T.W. Kim, Inkjet-printed photodetector arrays based on hybrid perovskite $CH_3NH_3PbI_3$ microwires, ACS Appl. Mater. Interfaces 9 (2017) 11662–11668.

[26] L. Li, Y. Deng, C. Bao, Y. Fang, H. Wei, S. Tang, F. Zhang, J. Huang, Self-filtered narrowband perovskite photodetectors with ultrafast and tuned spectral response, Adv. Opt. Mater. 5 (2017) 1700672.

[27] S. Li, S. Tong, J. Yang, H. Xia, C. Zhang, C. Zhang, J. Shen, S. Xiao, J. He, Y. Gao, B. Yang, J.-Q. Meng, High-performance formamidinium-based perovskite photodetectors fabricated via doctor-blading deposition in ambient condition, Org. Electron. 47 (2017) 102–107.

[28] Y. Zhang, J. Du, X.H. Wu, G.Q. Zhang, Y.L. Chu, D.P. Liu, Y.X. Zhao, Z.Q. Liang, J. Huang, Ultrasensitive photodetectors based on island-structured $CH_3NH_3PbI_3$ thin films, ACS Appl. Mater. Interfaces 7 (2015) 21634–21638.

[29] F. Zhao, K. Xu, X. Luo, W. Lv, Y. Peng, Y. Wang, F. Lu, S. Xu, Ultrasensitivity broadband photodetectors based on perovskite: research on film crystallization and electrode optimization, Org. Electron. 46 (2017) 35–43.

[30] Y. Wang, Q. Song, T. Lin, Y. Fue, X. Sun, B. Chu, F. Jin, H. Zhao, W. Li, Z. Su, Y. Li, Improved performance of $CH_3NH_3PbI_3$ based photodetector with a MoO_3 interface layer, Org. Electron. 49 (2017) 355–359.

[31] Y. Lee, J. Kwon, E. Hwang, C.H. Ra, W.J. Yoo, J.H. Ahn, J.H. Park, J.H. Cho, High-performance perovskite-graphene hybrid photodetector, Adv. Mater. 27 (2015) 41–46.

[32] Y. Wang, R. Fullon, M. Acerce, C.E. Petoukhoff, J. Yang, C. Chen, S. Du, S.K. Lai, S.P. Lau, D. Voiry, D. O'Carroll, G. Gupta, A.D. Mohite, S. Zhang, H. Zhou, M. Chhowalla, Solution-processed MoS_2/organolead trihalide perovskite photodetectors, Adv. Mater. 29 (2017) 1603995.

[33] T. Gao, Q. Zhang, J. Chen, X. Xiong, T. Zhai, Performance-enhancing broadband and flexible photodetectors based on perovskite/ZnO-nanowire hybrid structures, Adv. Opt. Mater. 5 (2017) 1700206.

[34] F. Cao, W. Tian, B. Gu, Y. Ma, H. Lu, L. Li, High-performance UV-vis photodetectors based on electrospun ZnO nanofiber-solution processed perovskite hybrid structures, Nano Res. 10 (2017) 2244–2256.

[35] Z. Zheng, F. Zhuge, Y. Wang, J. Zhang, L. Gan, X. Zhou, H. Li, T. Zhai, Decorating perovskite quantum dots in TiO_2 nanotubes array for broadband response photodetector, Adv. Funct. Mater. 27 (2017) 1703115.

[36] J.P.C. Baena, L. Steier, W. Tress, M. Saliba, S. Neutzner, T. Matsui, F. Giordano, T.J. Jacobsson, A.R.S. Kandada, S.M. Zakeeruddin, A. Petrozza, A. Abate, M.K. Nazeeruddin, M. Grätzel, A. Hagfeldt, Highly efficient planar perovskite solar cells through band alignment engineering, Energy Environ. Sci. 8 (2015) 2928–2934.

[37] J. Song, E. Zheng, J. Bian, X.F. Wang, W. Tian, Y. Sanehira, T. Miyasaka, Low-temperature SnO_2-based electron selective contact for efficient and stable perovskite solar cells, J. Mater. Chem. A 3 (2015) 10837–10844.

[38] W. Ke, D. Zhao, A.J. Cimaroli, C.R. Grice, P. Qin, Q. Liu, L. Xiong, Y. Yan, G. Fang, Effects of annealing temperature of tin oxide electron selective layers on the performance of perovskite solar cells, J. Mater. Chem. A 3 (2015) 24163–24168.

[39] Q. Jiang, L. Zhang, H. Wang, X. Yang, J. Meng, H. Liu, Z. Yin, J. Wu, X. Zhang, J. You, Enhanced electron extraction using SnO_2 for high-efficiency planar-structure $HC(NH_2)_2PbI_3$-based perovskite solar cells, Nat. Energy 2 (2016) 16177.

[40] Z. Zhu, Y. Bai, X. Liu, C.-C. Chueh, S. Yang, A.K.-Y. Jen, Enhanced efficiency and stability of inverted perovskite solar cells using highly crystalline SnO_2 nanocrystals as the robust electron-transporting layer, Adv. Mater. 28 (2016) 6478–6484.

[41] L. Huang, X. Sun, C. Li, J. Xu, R. Xu, Y. Du, J. Ni, H. Cai, J. Li, Z. Hu, J. Zhang, UV-sintered low-temperature solution-processed SnO_2 as robust electron transport layer for efficient planar heterojunction perovskite solar cells, ACS Appl. Mater. Interfaces 9 (2017) 21909–21920.

[42] K.-H. Jung, J.-Y. Seo, S. Lee, H. Shin, N.-G. Park, Solution-processed SnO_2 thin film for a hysteresis-free planar perovskite solar cell with a power conversion efficiency of 19.2%, J. Mater. Chem. A 5 (2017) 24790–24803.

[43] Q. Dong, Y. Shi, C. Zhang, Y. Wu, L. Wang, Energetically favored formation of SnO_2 nanocrystals as electron transfer layer in perovskite solar cells with high efficiency exceeding 19%, Nano Energy 40 (2017) 336–344.

[44] S. Chen, C. Teng, M. Zhang, Y. Li, D. Xie, G. Shi, A flexible UV–Vis–NIR photodetector based on a perovskite/conjugated-polymer composite, Adv. Mater. 28 (2016) 5969–5974.

[45] S. Tong, J. Sun, C. Wang, Y. Huang, C. Zhang, J. Shen, H. Xie, D. Niu, S. Xiao, Y. Yuan, J. He, J. Yang, Y. Gao, High-performance broadband perovskite photodetectors based on $CH_3NH_3PbI_3$/C8BTBT heterojunction, Adv. Electron. Mater. 3 (2017) 1700058.

[46] Q. Lin, A. Armin, R.C.R. Nagiri, P.L. Burn, P. Meredith, Electro-optics of perovskite solar cells, Nat. Photon. 9 (2015) 106–112.